Applied Surface Science 638 (2023) 157989

Contents lists available at ScienceDirect

Applied Surface Science

journal homepage: www.elsevier.com/locate/apsusc

Full Length Article

Structural reorganization of ultrathin g-C_3N_4 nanosheets for significantly boosting wide-spectrum-driven CO_2 photoreduction

Qian Zhang [a,1], Guangfu Liao [b,1], Bin Yang [a], Yan Zhang [a], Guixian Ge [c], Anna Lipovka [c], Jichang Liu [a], Raul D. Rodriguez [c,*], Xiaodong Yang [d,*], Xin Jia [a,*]

[a] School of Chemistry and Chemical Engineering/State Key Laboratory Incubation Base for Green Processing of Chemical Engineering, Shihezi 832003, PR China
[b] National Forestry and Grassland Administration Key Laboratory of Plant Fiber Functional Materials, College of Material Engineering, Fujian Agriculture and Forestry University, Fuzhou 350002, PR China
[c] Tomsk Polytechnic University, 30 Lenin Avenue, 634050 Tomsk, Russia
[d] Key Laboratory of Ecophysics and Department of Physics, College of Science, Shihezi University, Shihezi 832003, PR China

ARTICLE INFO

Keywords:
Photocatalysis
Carbon nitride
Structural reorganization
CO_2 photoreduction

ABSTRACT

Graphitic carbon nitride (g-C_3N_4) exhibits moderate CO_2 photoreduction due to fast recombination of photo-excited charges and low-grade visible light absorption. Herein, we synthesized highly polymerized ultrathin g-C_3N_4 nanosheets by structural reorganization. Both experimental and theoretical calculations indicate that amino groups stabilized by hydrogen bonding networks are the easiest to remove to form a more stable bridged N-$(C)_3$. This procedure provides additional electron transfer channels with an extended conjugated $\pi \rightarrow \pi^*$ system and buckled plane structure with activated $n \rightarrow \pi^*$ electronic transitions. This new configuration significantly improves the separation efficiency of photoexcited charges and widens the light absorption range. As a result, the prepared g-C_3N_4 shows efficient CO_2-to-CO conversion with a CO production rate of 12.95 μmol g^{-1} h^{-1} under $\lambda \geq 420$ visible light and 2 μmol g^{-1} h^{-1} under $\lambda \geq 500$ visible light, respectively. This work offers a new design idea for highly active visible-light-driven g-C_3N_4 for CO_2 photoreduction.

1. Introduction

Excessive CO_2 emissions from non-renewable energy sources raised significant environmental challenges and threats, affecting humanity's future [1]. The conversion of CO_2 into fuels or other valuable chemicals using photocatalysis is one of the most desired strategies to reduce the negative impact [2–8]. Given the inherent thermodynamic stability and kinetic inertness of CO_2 molecules, photocatalysts are needed to reduce the reaction potential barrier and accelerate the reaction kinetics of CO_2 photoreduction [9–13]. Although inorganic semiconductor photocatalysts have been developed intensively in the past decade, they are still insufficient for large-scale practical applications, partly because of low selectivity and production rate. Polymeric graphitic carbon nitride (g-C_3N_4) is an intriguing photocatalyst thanks to its earth-abundant nature, easy and low-cost preparation, and excellent stability, satisfying the thermodynamic requirements for CO_2 photoreduction [14,15]. However, some intrinsic drawbacks, including poor electron mobility, low specific surface area, and narrow light absorption range, restrict g-C_3N_4 photocatalytic performance [16,17]. Therefore, g-C_3N_4 engineering to achieve rapid and effective photoexcited charge transfer and separation, highly exposed active sites, and broad visible light absorption is still a critical challenge for CO_2 conversion and utilization.

Conventional g-C_3N_4 synthesis approaches remain within solid-phase thermal polymerization using nitrogen-rich precursors [18]. Due to the limited liquidity of the reaction intermediates, the heptazine-based molecular chain is not fully polymerized, resulting in amino (NH_1 and NH_2) groups on the heptazine ring units, which are stabilized by hydrogen-rich bonding networks [19,20]. However, the photoexcited charges have a preferential transport in the in-plane direction along the heptazine-based chain without hydrogen-bond networks, as confirmed by the works of Liu et al. [21] and Zhang et al. [22]. Using covalent bonds instead of intramolecular hydrogen bonds would effectively improve the separation and transfer of photoexcited charges. For instance, Wang et al. prepared a series of highly polymerized crystalline g-C_3N_4 by removing the hydrogen bond networks with the aid of molten salts [23–25]. Compared with the molten salt method, the simple and

* Corresponding authors.
E-mail addresses: raul@tpu.ru (R.D. Rodriguez), yangxiaodong1209@hotmail.com (X. Yang), jiaxin@shzu.edu.cn (X. Jia).
[1] These two authors contributed equally to this work.

https://doi.org/10.1016/j.apsusc.2023.157989
Received 20 May 2023; Received in revised form 27 June 2023; Accepted 6 July 2023
Available online 17 July 2023

green post-annealing process can not only remove the hydrogen bond networks and improve the polymerization of g-C_3N_4 but also distort the planar structure of g-C_3N_4 resulting in the activation of n → π* electron transitions and broadening visible light absorption [26–30]. In contrast, other studies have indicated that the enhanced photocatalytic performance of g-C_3N_4 can be attributed to the introduction of nitrogen defects through post-annealing [31,32]. Therefore, the "structural reorganization" of g-C_3N_4 by post-annealing remains a topic of debate, with conflicting views. Furthermore, studies on post-annealed g-C_3N_4 have primarily focused on photocatalytic hydrogen [26–31] and H_2O_2 production [32], while research on its application in CO_2 photoreduction and the expansion of visible light absorption range is limited. Consequently, understanding the structural reorganization of g-C_3N_4 through post-annealing and its relationship with CO_2 photoreduction in a broad range of light absorption remains elusive. This knowledge gap necessitates urgent investigation, which is the primary objective of this study. In this work, g-C_3N_4 nanosheets (UCN) rich with amino groups stabilized via hydrogen-bonding networks are firstly prepared by polymerizing an aqueous urea solution at high temperatures. Density functional theory (DFT) calculations show that the amino groups stabilized by hydrogen bonding networks are the least stable. Meanwhile, the bridged N-$(C)_3$ formed after removing the amino group has the highest stability compared with other nitrogen atoms in the heptazine structure. Based on the insights from DFT calculations, we post-annealed g-C_3N_4 at different temperatures under argon atmosphere protection to remove amino groups and form the bridged N-$(C)_3$. The newly-formed bridged N-$(C)_3$ interconnects the heptazine units opening new channels for electron transfer with an extended conjugated π → π* system and introducing distortions to the plane structure, activating n → π* electronic transitions. This structural reorganization leads to rapid and effective photoexcited charge transfer and separation as well as broadening visible light absorption. The amino group removal is further converted into NH_3 gas. The release of NH_3 gas results in the exfoliation of UCN, generating highly exposed active sites and reducing the perpendicular migration distance of charges to the surface. As expected, the UCN-620 photocatalyst demonstrates an efficient conversion rate of CO_2 to CO (12.95 μmol g^{-1} h^{-1}) under λ ≥ 420 nm visible light, which is threefold that of UCN. Meanwhile, the conversion rates of CO_2 to CO exceed 2 μmol g^{-1} h^{-1} over UCN-620 under visible light excitation λ ≥ 500 nm, which is practically impossible to reach with the original UCN.

2. Experimental section

2.1. The preparation of UCN

The covered corundum crucible containing 50 mL of 400 g/L aqueous urea was calcined at 550 °C for 4 h at 5 °C/min in a muffle furnace. The obtained light-yellow powders were denoted as UCN.

2.2. The preparation of UCN-X

The covered corundum crucible containing 0.2 g of UCN was calcined at specified temperatures for 2 h at 5 °C/min in a tube furnace under argon gas protection. The obtained powders were denoted as UCN-X (X = 580–640 °C; where X represents the pyrolysis temperature).

2.3. Photocatalytic CO_2 reduction

The CO_2 photoreduction was acquired on an on-line analytical system (Labsolar-III, PerfectLight, Beijing), which was linked to gas chromatography (GC D7900P, TCD detector, Ar as a carrier gas, 5 Å molecular sieve column, Shanghai Tech comp). The 30 mg of photocatalyst were dispersed in 8 mL of 10 vol% triethanolamine (TEOA) aqueous solution. A 300 W Xenon lamp with an optical filter (λ > 420, 500, or 550 nm) was used as the light source. The reaction cell was evacuated for 1 h to remove the air completely. After degassing, the reactor cell was filled with CO_2 (99.999%, 1 atm). The CO_2 photoreduction was measured every hour under illumination. The amount of CO and CH_4 gas was detected by gas chromatography. The quantum efficiency (QE) of CO_2 photoreduction was measured under 420 nm monochromatic light, and the QE values were calculated according to the following equation:

$$QE(\%) = \frac{number\ of\ reacted\ electeds}{number\ of\ incident\ photons} \times 100\% = \frac{number\ of\ CO\ molecules \times 2}{number\ of\ incident\ photons} \times 100\%$$

2.4. Photocatalytic H_2 production

The photocatalytic H_2 production was acquired on an on-line analytical system (Labsolar-III, PerfectLight, Beijing). The optimal catalyst mass (30 mg) was dispersed in 100 mL of 10 vol% TEOA aqueous solution, and 3 wt% Pt was in-situ photodeposited on the surface of photocatalysts by adding H_2PtCl_6. A 300 W Xenon lamp with/without a UV-cutoff filter (λ > 420 nm) was used as the light source. Before photocatalytic HER began, the reaction cell was evacuated for 1 h to remove the air completely. The amount of H_2 gas produced was detected by gas chromatography.

2.5. Photoelectrochemical measurement

The electrochemical measurements were recorded on a CHI 760D electrochemical workstation with a standard three-electrode system under visible light irradiation (PLS-SXE 300C (BF); PerfectLight, Beijing). The saturated Ag/AgCl electrode, Pt foil, and ITO/glass sheet coated with 0.5 mg of catalyst were conducted as a reference electrode, a counter electrode, and a working electrode, respectively.

2.6. Sample characterization

Powder X-ray diffraction (XRD) measurements were collected on a Rigaku D/MAX-RB diffractometer with monochromatic Cu Kα radiation (λ = 0.15418 nm). X-ray photoelectron spectra (XPS) were recorded on a VG EscaLab 220i spectrometer using a standard Al Kα X-ray source (300 W) and analyzer pass energy of 20 eV. Atomic force microscopy (AFM) images were obtained using a Dimension 3100 from Veeco, USA. Scanning electron microscopy (SEM) images were recorded on an FEI Quanta 250 FEG instrument. High-resolution transmission electron microscopy (HRTEM) images were recorded on a JEM-2100 electron microscope (JEOL, Japan). The reflectance spectra of all samples over the 190–1000 nm range were obtained by A UV–visible spectrometer equipped with a Labsphere diffuse reflectance accessory (UV-2550, Shimadzu, Japan), using $BaSO_4$ as the reference standard. Fourier transform infrared (FTIR) spectra were collected on a Bruker spectrometer (spectrum 2000) over the frequency range 2000–450 cm^{-1} at a resolution of 4 cm^{-1}. Solid-state ^{13}C magic angle spinning (MAS) NMR measurements were acquired on a Bruker AVANCE III 400 MHz WB solid-state NMR spectrometer. The specific surface area analysis of all samples was obtained by using an N_2 adsorption–desorption instrument (BET, ASAP2020, USA). The photoluminescence (PL) spectra and time-resolved PL (TRPL) spectra were recorded by using an Edinburgh FLS980 spectrophotometer and the excitation wavelength is set to 380 nm. An organic element analyzer was acquired on elementar vario EL cube, Germany. In situ diffuse reflectance infrared Fourier transform (DRIFT) results were provided by a Nicolet iS50 FTIR spectrometer. Temperature-programmed chemisorption analyzer (TPD) was acquired on an AutoChem1 II 2920.

2.7. Computation

DFT calculations were acquired within the General Gradient

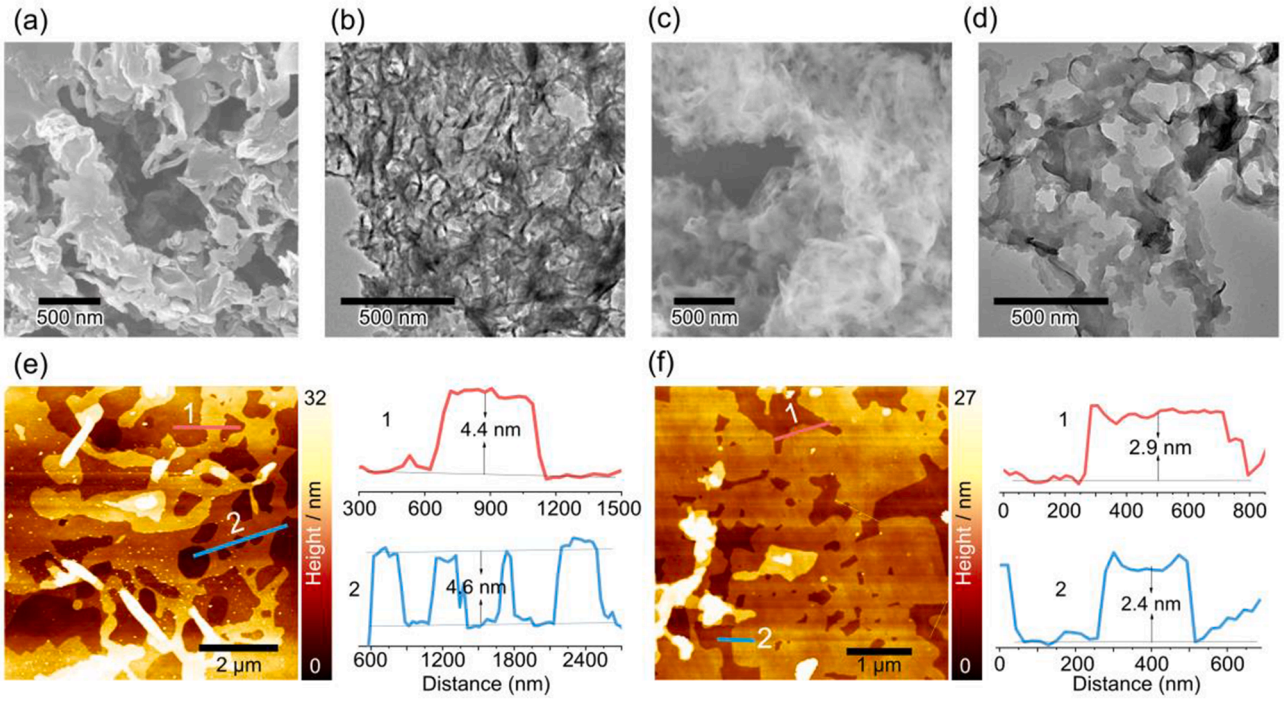

Fig. 1. SEM and TEM of UCN (a, b) and UCN-620 (c, d); AFM images and corresponding height profiles of UCN (e) and UCN-620 (f), respectively.

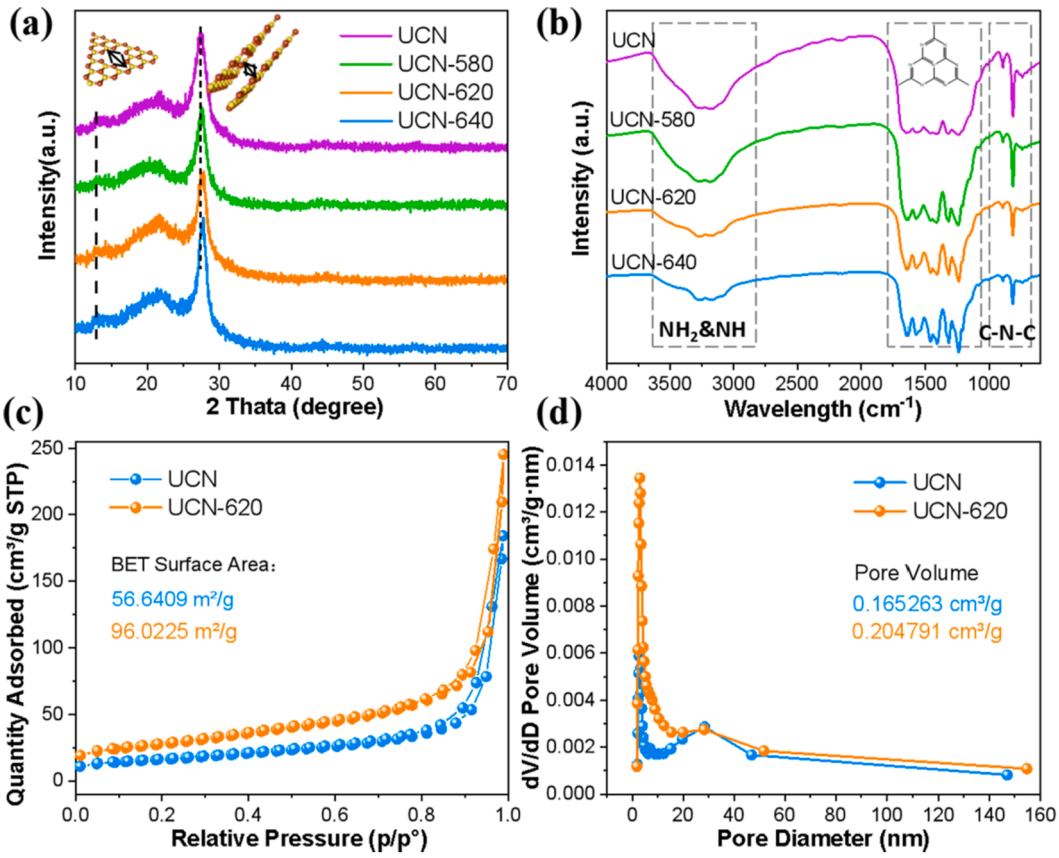

Fig. 2. (a) XRD patterns and (b) FTIR spectra of UCN, UCN-580, UCN-620, and UCN-640; (c) N_2 adsorption–desorption isotherms, (d) the corresponding PSD curves of UCN and UCN-620.

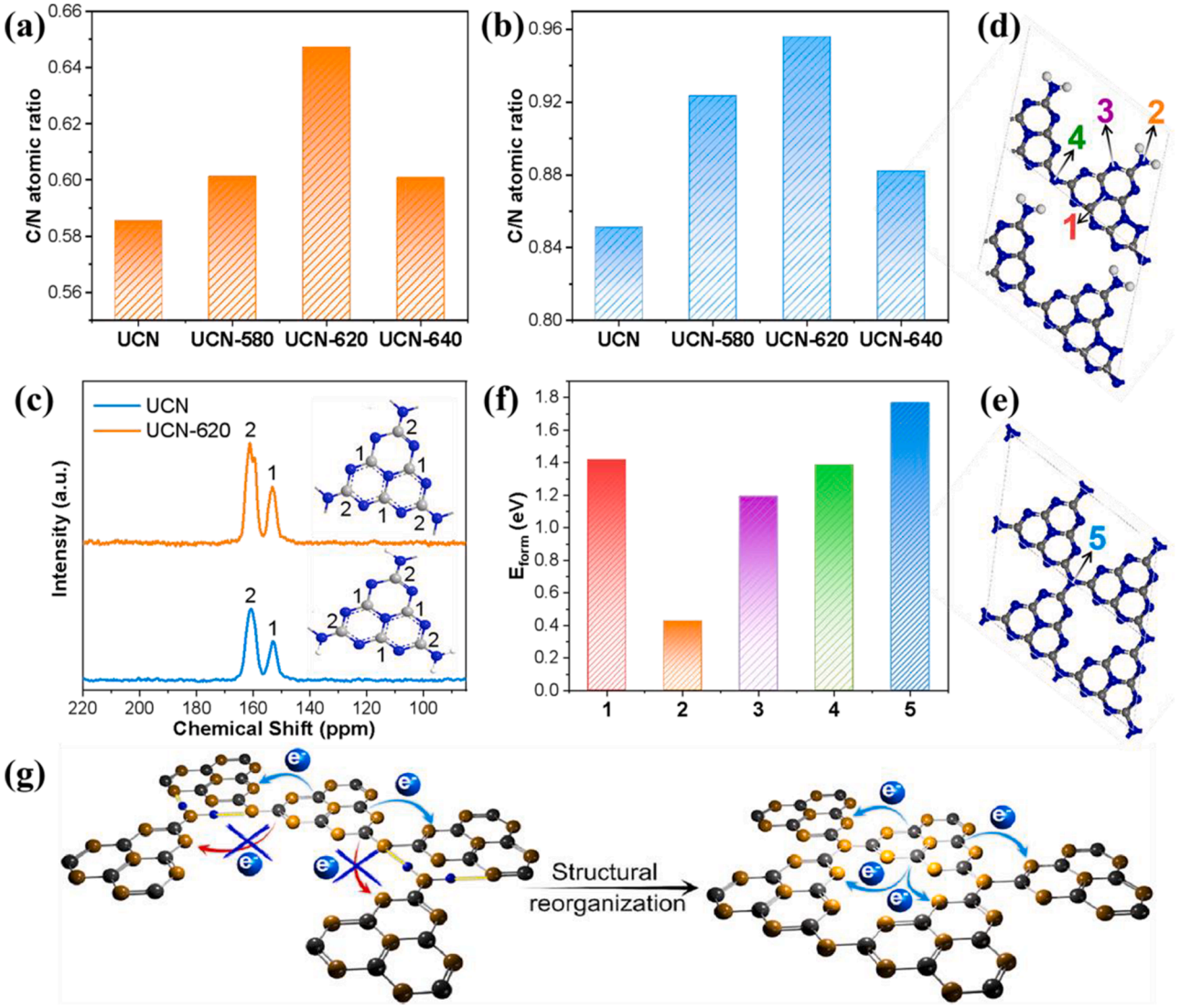

Fig. 3. The C/N atomic ratio was obtained by (a) organic element analysis and (b) XPS surface element analysis of different samples: UCN, UCN-580, UCN-620, and UCN-640; (c) ^{13}C solid-state NMR of UCN and UCN-620; Model structure [21,24] of UCN (d) and model structure of UCN-620 (e) as well as (f) corresponding E_{form} of nitrogen atoms in different positions; (g) Schematic illustration of g-C_3N_4 structural reorganization.

Approximate (GGA) functional using the plane-wave-based Vienna Ab-initio Simulation Package (VASP) code. The vacuum space is set to 20 Å, which has been proven large enough to avoid the layer-to-layer effects. The cutoff energies for plane waves are 500 eV. A 6 × 6 × 1 Monkhorst-Pack k-point mesh is used in the geometry optimization and geometries of the composites are optimized separately until the force on each atom is less than 10^{-4} eV $Å^{-1}$.

3. Results and discussion

3.1. Structural characterization at the molecular level

The morphology of prepared samples before and after post-annealing was analyzed by SEM, HRTEM, and AFM. Water acts as a gas template to peel off and overcome the strong interaction between g-C_3N_4 layers in the polymerization of aqueous urea solution, generating UCN nanosheets (Fig. 1a, b). The thickness of UCN nanosheets contains about 12–13 layers based on the 0.35 nm thickness of the monolayer g-C_3N_4 (Fig. 1e) [32]. Due to the stripping function of NH_3 released under high temperatures, the morphology of UCN-620 prepared by post-annealing is different (Fig. 1c, d). Fig. 1f shows that UCN-620 is an ultrathin nanosheet comprising 6–7 layers of g-C_3N_4. Thus, we confirm that in-situ NH_3 production at a high temperature can effectively achieve UCN exfoliation.

XRD patterns were used to characterize the crystal structure of the samples. All samples have the (1 0 0) and (0 0 2) planes of g-C_3N_4 at 13.2° and 27.39° (JCPDS 87–1526) [33], which represents in-plane repeated units of heptazine and interlayer stacking of π-conjugated C-N heterocycles, respectively (Fig. 2a). The peak intensity of UCN at the (0 0 2) plane did not decrease but increased slightly and moved to a higher angle with the increase of pyrolysis temperature under argon protection. These results indicate that post-annealing can significantly promote the polymerization of UCN and peel it off into thinner nanosheets [34]. Although the degree of polymerization and crystallinity of UCN-620 obtained by structural reorganization is improved, no noticeable lattice fringes appear (Figure S2), which are attributed to the formation of bridged N-$(C)_3$, resulting in the distorted plane structure. XPS analysis shows that high pyrolysis temperatures have no apparent effect on the samples' elemental composition (Figure S3). FTIR spectra were used to characterize changes in functional groups on the samples' surface [35]. As shown in Fig. 2b, the NH_1/NH_2 peak intensity between 2900 and 3600 cm^{-1} in g-C_3N_4 gradually decreases with the increase of pyrolysis

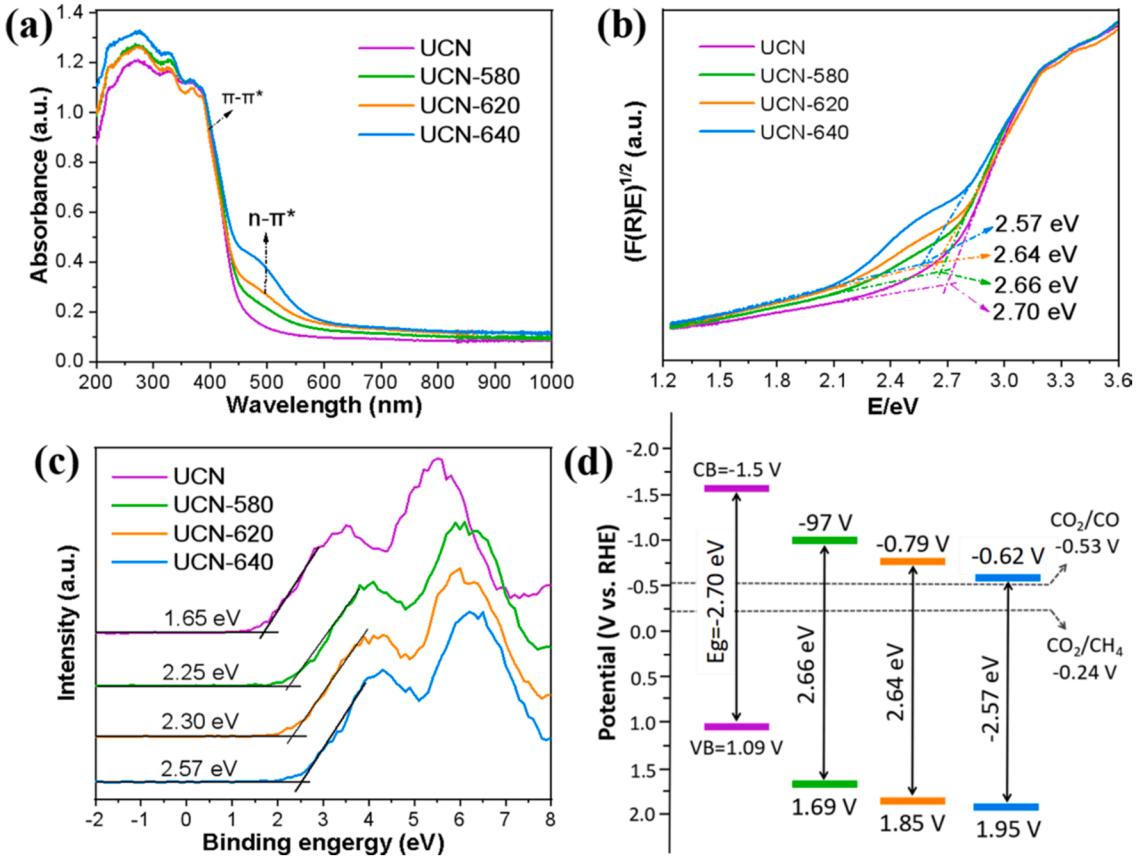

Fig. 4. (a) UV–Vis diffuse reflectance spectra, (b) bandgaps structure spectra, (c) VB-XPS spectra and (d) schematic energy band structures of different samples: UCN, UCN-580, UCN-620, and UCN-640.

temperature. This indicates that NH_1/NH_2 stabilized by hydrogen bonding networks in g-C_3N_4 breaks up at high temperatures. The generated NH_3 gas can realize the in-situ stripping of g-C_3N_4. As shown with BET results in Fig. 2c, the NH_3 released under high temperatures can further promote the exfoliation of UCN, resulting in a significantly enlarged specific surface area (by 69.5%). The pore size distribution results in Fig. 2d show that the surface of UCN-620 obtained by post-annealing has a larger number of mesopores and macropores than UCN.

XPS spectra were used to elucidate the structural reorganization of g-C_3N_4 resulting from post-annealing. As shown in Fig. S4a, all samples show three characteristic XPS peaks located at 398.64, 399.59, and 401.19 eV in the fitted N 1s spectra, which are assigned to sp^2-hybridized nitrogen atoms in heptazine rings (C-N═C), tertiary nitrogen N-$(C)_3$ groups, and –NH_2 groups, respectively [35,36]. With the increase in post-annealing temperature, the stable NH_2 groups with hydrogen bond networks are removed, and the peak area ratio decreases drastically in agreement with FTIR results (Fig. S4b). At the same time, the peak area of bridged N-$(C)_3$ increases significantly (Fig. S4b). These critical analytical results imply that the carbon on the heptazine units that lost its NH_2 group overcomes steric hindrance and undergoes a carbon–nitrogen coupling reaction with the –NH group connecting two heptazine units to form a more stable bridged N-$(C)_3$ as predicted by DFT calculations. When the post-annealing temperature exceeds 620 °C, the stable amino group with hydrogen bond network and the bridged N-$(C)_3$ formed subsequently do not change much anymore, indicating that the surface structural reorganization is almost done, ending up with the destruction of the surface structure.

Organic elemental analysis is an intuitive quantitative method to characterize the C/N elemental ratio in g-C_3N_4. Fig. 3a shows that below 620 °C, the C/N elemental ratio increases significantly with the increase of pyrolysis temperature. The C/N value closer to 3/4 states that the structural reorganization substantially enhances the degree of UCN polymerization [37,38]. We also used XPS as a highly sensitive surface analysis method to characterize C/N ratio changes caused by structural reorganization (Fig. 3b) [39]. The variation trend of the C/N elemental ratio gained from XPS analysis as a function of pyrolytic temperature is consistent with the results obtained from organic elemental analysis. Due to the surface-sensitive nature of XPS, the C/N ratio change is more evident from XPS than from organic elemental analysis, which indicates that the structural reorganization occurs mainly on the g-C_3N_4's surface. In addition, the ratio of C/N for UCN-620 is approximately 1, indicating a C-rich g-C_3N_4 has been formed on the outer surface (see Fig. 3b). However, the ratio of C/N for UCN-620 is approximately 0.75, which means that the UCN-620's structure is C-rich outside and N-rich inside (see Fig. 3a). When the post-annealing temperature exceeds 620 °C, the C/N elemental ratio in g-C_3N_4 deduced from organic element analysis and XPS does not increase continuously but decreases after reaching a maximum. We attribute this non-monotonic behavior to the breakage of the heptazine structure in g-C_3N_4 when the temperature exceeds 620 °C. Meanwhile, ammonium ions due to the release of NH_3 were detected in water by ion chromatography. Combining this finding with FTIR, XRD, XPS, and elemental analysis, we conclude that the amino groups stabilized by the hydrogen bond networks get removed at high temperatures. Then, the carbon on the heptazine units without the amino group can overcome steric hindrance and undergo a carbon–nitrogen coupling reaction with the NH connecting two heptazine units. As a result, a more stable bridged N-$(C)_3$ is formed, resulting in an enhanced degree of surface polymerization. ^{13}C solid-state NMR of analyzed samples was used to prove further the structural reorganization process of UCN (Fig. 3c) [40–42]. There are two strong peaks located at the C1 atom (165.27 ppm) and C2 atom (157.38 ppm), corresponding to the chemical shifts of $C_{2N\text{-}NHx}$ and C_{3N} in the corrugated g-C_3N_4 frameworks,

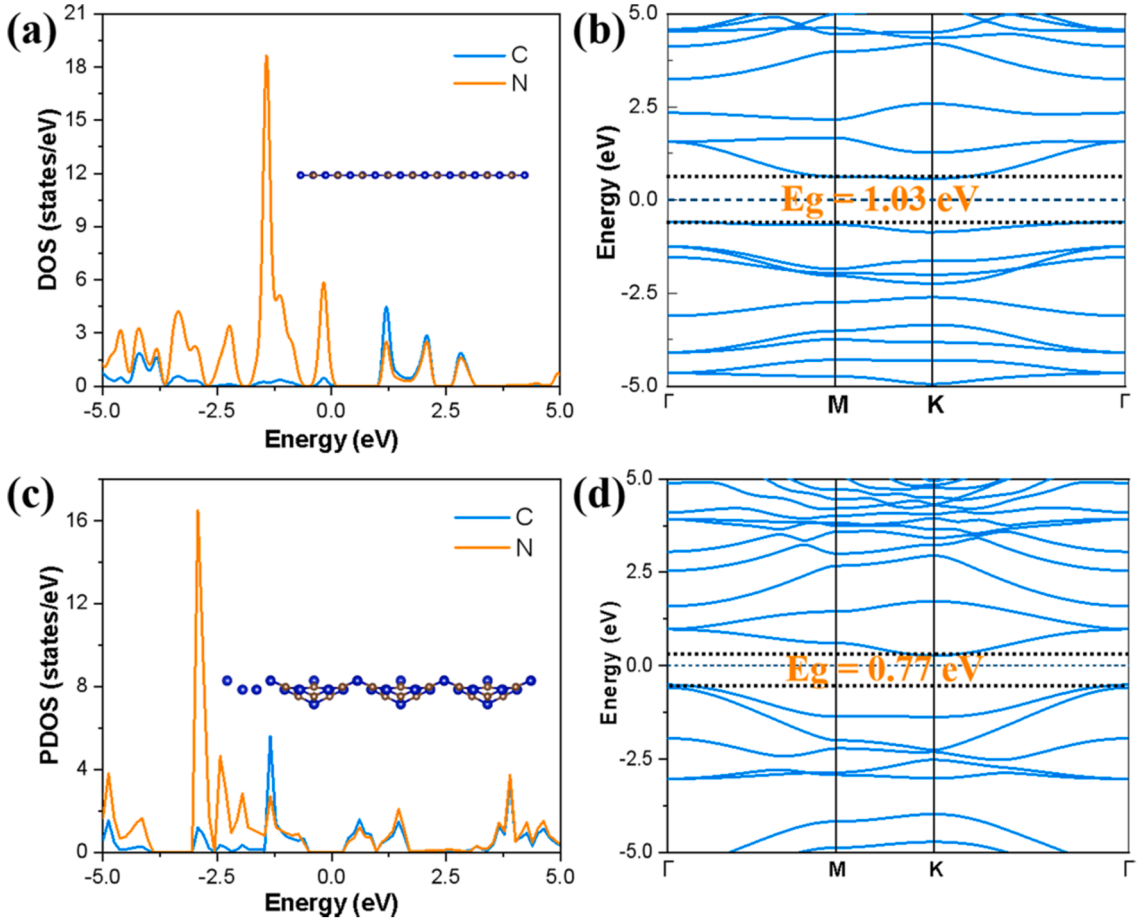

Fig. 5. Calculated DOS (a, c) and corresponding band structure (b, d) of g-C_3N_4 with a planar structure and g-C_3N_4 with a distorted planar structure, respectively (insets in (a) and (c): atomic structure model of g-C_3N_4 with a planar structure and a distorted planar structure, respectively).

respectively. Compared with UCN, the ^{13}C solid-state NMR of UCN-620 shows a higher peak intensity, possibly due to the high polymerization caused by structural reorganization.

To further complement the structural reorganization of UCN occurring at high temperatures, we calculated each nitrogen atom formation energy (E_{form}) by DFT. As shown in Fig. 3d-f, the formation energies (E_{form}) of '1', '2', '3', and '4' positions are 1.417, 0.425, 1.192, and 1.385 eV, respectively. The results confirm that the NH_2 groups stabilized by hydrogen bond networks at position '2' are the most unstable and easy to remove. When UCN is polymerized to UCN-620 by post-annealing, the resulting bridged N-$(C)_3$ formed at position '5' has a maximum E_{form} of 1.767 eV, indicating that the bridged N-$(C)_3$ is the most stable. In short, we can assume that the $–NH_2$ groups stabilized by the hydrogen bonding networks in g-C_3N_4 can be removed and form a more stable bridged N-$(C)_3$ at high temperature without breaking the heptazine structural units.

Based on the analysis above, the structural reorganization of UCN is given in Fig. 4g. The DFT calculations and experimental results show that the amino groups stabilized by hydrogen bond networks can be removed by simple heating, forming a stable bridged N-$(C)_3$, which extends the π-conjugated system making more electron transfer channels available. This is essential for an outstanding photogeneration of charge carriers with enhanced transfer and separation.

3.2. The light absorption and well-tuned band structures of samples

UV–Vis diffuse reflectance spectra (UV–Vis DRS) were used to analyze the samples' light absorption and optical bandgap [43,44]. As shown in Fig. 4b, the bandgaps derived from UV–Vis DRS (Fig. 4a) slightly decrease in a controlled manner with increasing pyrolysis temperatures, attributed to the structural reorganization of g-C_3N_4. The samples' electronic structure was investigated from the valence band XPS spectra ($E_{VB\text{-}XPS}$), revealing a decrease in UCN as the pyrolysis temperature increased (Fig. 4c). The formula ($E_{VB} = \Phi + E_{VB\text{-}XPS} - 4.44$) was used to determine the valence band position (E_{VB}) versus normal hydrogen electrode (NHE) at pH = 7, where $\Phi = 3.88$ eV is the analyzer electron work function [44]. Combining bandgaps and E_{VB} values, the adjustable band structure of UCN is achieved by controlling the pyrolysis temperatures (see Fig. 4d). The continuously adjustable oxidation potential provides a strong driving force for triethanolamine (TEOA) oxidation. This is critical because a rapid TEOA oxidation provides more electrons for CO_2 photoreduction. It is worth noting that UCN-620 presents a significant red shift of photoabsorption (Fig. 4a). This may be attributed to the distortion of the g-C_3N_4 plane structure caused by the bridged N-$(C)_3$, originating from n → π* electronic transitions [28,29]. At the same time, the pyrolysis temperature can control these n → π* transitions well.

Density of states (DOS) calculations by DFT were used to obtain further insights on the significant red shift of photoabsorption attributed to the distortion of g-C_3N_4's plane structure caused by bridged N-$(C)_3$. Fig. 5 presents the band structure evolution obtained from DFT calculations for two g-C_3N_4 configurations: one with a planar structure and the other with a distorted planar structure. The DOS calculation and band structure show that the composition of the conduction band arises due to contributions from C 2p and N 2p orbitals. Meanwhile, the composition of the valence band is mainly ascribed to N 2p orbitals (Fig. 5a and b). These observations are in agreement with a previous report [38]. Fig. 5b and d show that the g-C_3N_4's bandgap with a

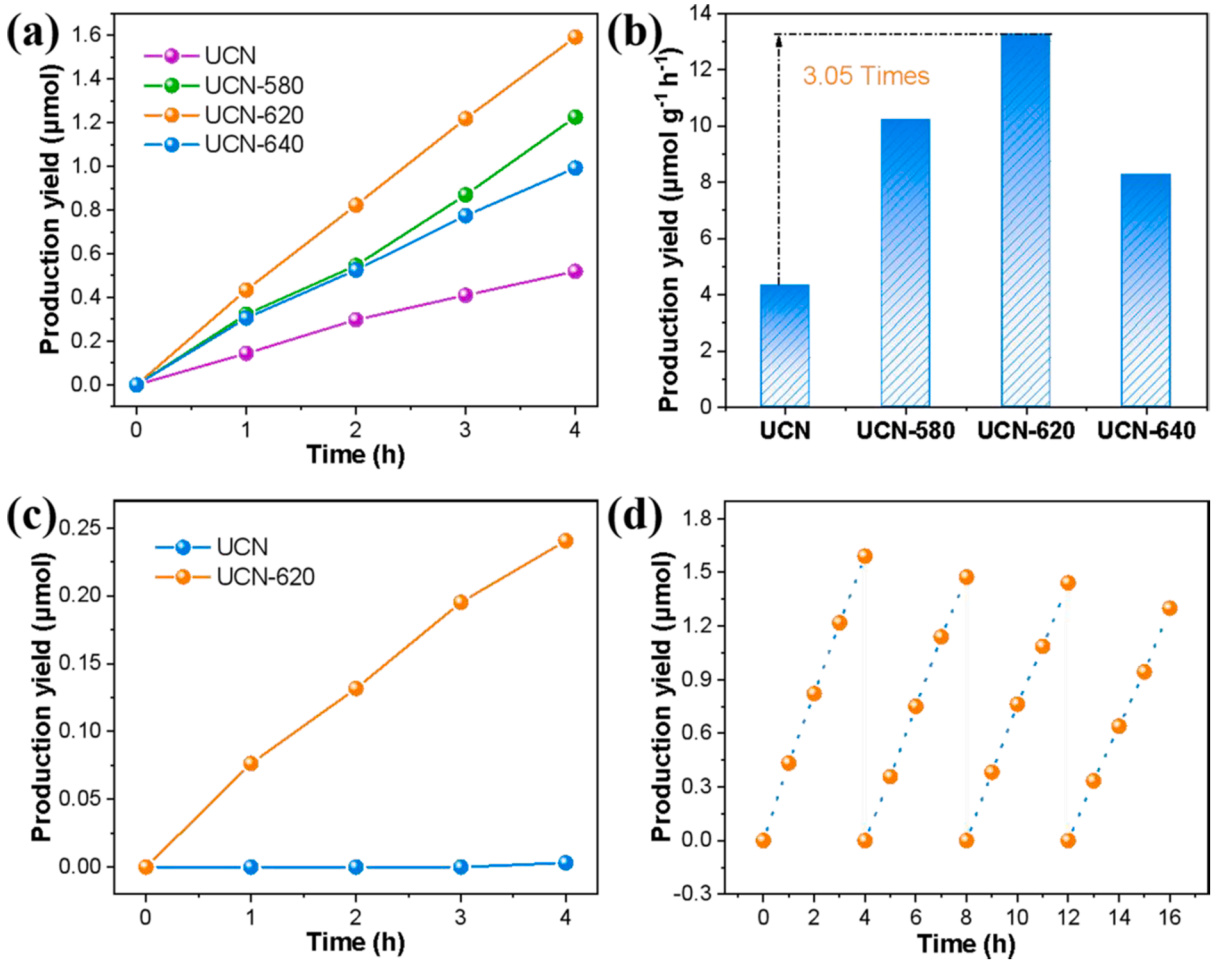

Fig. 6. (a) The CO_2 photoreduction to CO performance and (b) corresponding rate over UCN-620 and UCN under $\lambda \geq 420$ nm visible light; (c) The CO_2 photoreduction to CO performance over UCN-620 and UCN under $\lambda \geq 500$ nm visible light; (d) Stability test for UCN-620 under $\lambda \geq 420$ nm visible light.

distorted planar structure is significantly smaller than that of g-C_3N_4 with a planar structure. This gives strong evidence for the significant red shift of photoabsorption through the distortion of the g-C_3N_4's planar structure due to the formation of bridged N-$(C)_3$, resulting in activated n → π* electronic transitions.

3.3. *Efficient photocatalytic CO_2 reduction*

CO_2 photoreduction was performed to evaluate the photocatalytic properties of the samples under the condition of TEOA as a sacrificial agent. We investigated the impact of the extended conjugate π → π* system and activated n → π* electron transitions to CO_2 photoreduction activity. We performed experiments under different excitation wavelengths in the visible range, $\lambda \geq 420$ nm, $\lambda \geq 500$ nm, and $\lambda \geq 550$ nm. As shown in Fig. 6a, the UCN photocatalyst exhibits a sustained and weak CO_2 to CO photocatalytic reduction over four hours, giving only trace amounts of CH_4 (Fig. S5a), while the elevation of pyrolysis temperature promotes the photocatalytic reduction. The CO_2 to CO conversion rate for UCN-620 reaches its highest value of 12.95 μmol g^{-1} h^{-1}, threefold that of the pristine UCN (Fig. 6b). When the pyrolysis temperature reaches 640 °C, the CO_2 photoreduction performance degrades because of the broken heptazine rings and reduced reduction potential. The QE of CO_2 photoreduction of UCN-620 reached 0.0025% under 420 nm monochromatic light. As shown in Fig. S6a, using TiO_2 Degussa P-25 (P25) as the benchmark catalyst, the CO obtained from CO_2 photoreduction gradually accumulates with the increase of illumination time. Compared to P25, UCN-620 exhibits more significant CO_2 photoreduction performance under visible light (Fig. S6b). These exciting results show that UCN-620 is a better CO_2 photoreduction than P25 under visible light. We showed that in the absence of co-catalysts and photosensitizers, when a hole sacrificial agent is present, UCN-620 has a more significant activity of CO_2 photoreduction compared with some photocatalysts reported so far, including the g-C_3N_4 ones (see Table S1).

To further demonstrate the contribution of n → π* electronic transitions to CO_2 photoreduction, we change the visible light excitation source from $\lambda \geq 420$ nm to $\lambda \geq 500$ nm in the visible light spectrum. The CO_2 to CO conversion rate for UCN-620 can still reach a rate of 2 μmol g^{-1} h^{-1} (Fig. 6c). Such extraordinary performance and selectivity are practically impossible with the conventional UCN. The main reason for these remarkable differences is that the wide bandgap of UCN hinders the absorption of photons with $\lambda \geq 500$ nm, resulting in weaker CO_2 photoreduction. The UCN-620 can even achieve CO_2 photoreduction under $\lambda \geq 550$ nm visible light (Fig. S5c), which does not happen for UCN without activated n → π* electronic transitions. Those results show that n → π* transitions have high efficiency for CO_2 photoreduction to produce CO. Moreover, there was a slight attenuation in the CO_2 photoreduction performance after 16 h of reaction (Fig. 6d), which is attributed to TEOA consumption in the solution during the reaction [45,46]. In the absence of TEOA as a hole sacrificial agent, UCN-620 still induces CO_2 photoreduction to CO (Fig. S7a), but the activity of photoreduction is still not sufficient compared to the results with TEOA (Fig. S7b). A control experiment was conducted to confirm that the C sources are derived from CO_2 photoreduction (see Fig. S5d). When the

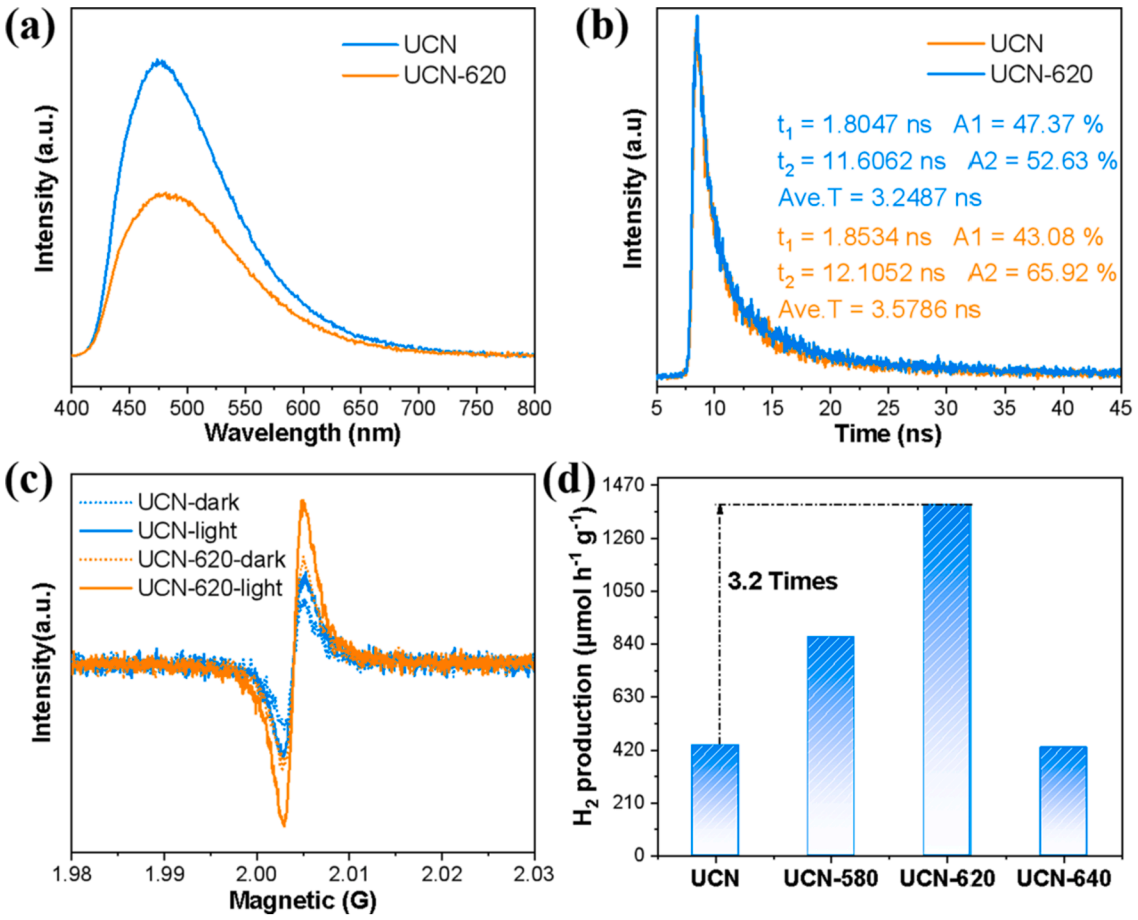

Fig. 7. (a) Steady-state PL spectra, (b) time-resolved PL decay spectra and (c) EPR results of UCN and UCN-620; (d) Photocatalytic H_2 evolution of samples under visible light ($\lambda \geq 420$ nm).

CO_2 atmosphere was replaced by argon, neither CO was detected under visible light excitation ($\lambda \geq 420$ nm), strongly confirming that CO was generated from CO_2 photoreduction rather than from the decomposition of UCN-620 or the photocatalytic degradation of TEOA. Chen et al. conducted ^{13}C isotope labeling experiments under the same experimental conditions, and the results also showed that the produced CO come from the CO_2 photoreduction[21]. Those results indicate that UCN-620 has outstanding CO_2 photoreduction activity, excellent photocatalytic stability, and selectivity in a wide light absorption range.

3.4. *Efficient separation and transfer of photoexcited charges*

The PL and TRPL are investigated to elucidate the significant promotion in separation, transfer, and lifetime of photoexcited charges due to the structural reorganization of g-C_3N_4. The UCN-620 has significantly reduced PL intensity compared to UCN, implying that the rapid recombination of photoexcited charges can be suppressed continuously (Fig. 7a) [47,48]. Notably, PL peaks of UCN-620 are wider than UCN due to activated $n \rightarrow \pi^*$ transitions after the formation of bridged N-$(C)_3$ with a buckled planar structure in agreement with UV–Vis DRS results [27,49]. The average lifetimes of photoexcited charges for UCN and UCN-620 reflected by TRPL are 3.24 and 3.56 ns, respectively (Fig. 7b), which indicates that the lifetime of photoexcited charges can be extended by structural reorganization of UCN, resulting in increasing the probability of photocatalytic oxidation and reduction reactions, as well as promoting photocatalytic activity [49]. The UCN-620 photocatalyst shows the most remarkable photocurrent response, which reflects that structural reorganization can inhibit the internal recombination of electrons and holes (Figure S8a). The electrochemical impedance of UCN-620 presents the smallest diameter of the semicircular Nyquist curves, which means that the structural reorganization of UCN reduces the transfer resistance of photoexcited charges (Figure S8b) [45]. The EPR was used to confirm the presence of unpaired electrons on the photocatalyst's surface. Compared with the UCN, the UCN-620 shows higher EPR signal intensity than UCN in the presence or absence of illumination (Fig. 7c), which is ascribed to local stress and bond-angle disorder in the connective bridged N-$(C)_3$ structure, resulting in rich surface unpaired electrons [50,51]. These unpaired electrons can accelerate the generation of photoexcited charges [43].

To reflect further the utilization efficiency of photogenerated charges, we evaluated the photocatalytic hydrogen production of all our samples (Fig. 7d). For UCN, this value is relatively high (439 μmol $g^{-1}h^{-1}$) in consideration of the template and stripping function of water [52]. However, by increasing pyrolysis temperature, the photocatalytic hydrogen production is significantly enhanced by reaching rate values for UCN-620 as high as 1400 μmol $g^{-1}h^{-1}$, 2.8 times higher than for the conventional UCN. This excellent photocatalytic hydrogen production of UCN-620 originates from the high utilization efficiency of photogenerated charge carriers, which also translates into a high efficiency for CO_2 photoreduction showing the same tendency. Compared with reported C-rich g-C_3N_4, UCN-620 has a better activity of photocatalytic H_2 production (see Table S2), also indicating that UCN-620 may have better photocatalytic performance for CO_2 photoreduction.

3.5. *CO_2 photoreduction mechanism*

It is reported that the Lewis bases in the heptazine rings of g-C_3N_4 can act as the adsorption sites of CO_2 molecules and form carbamate with

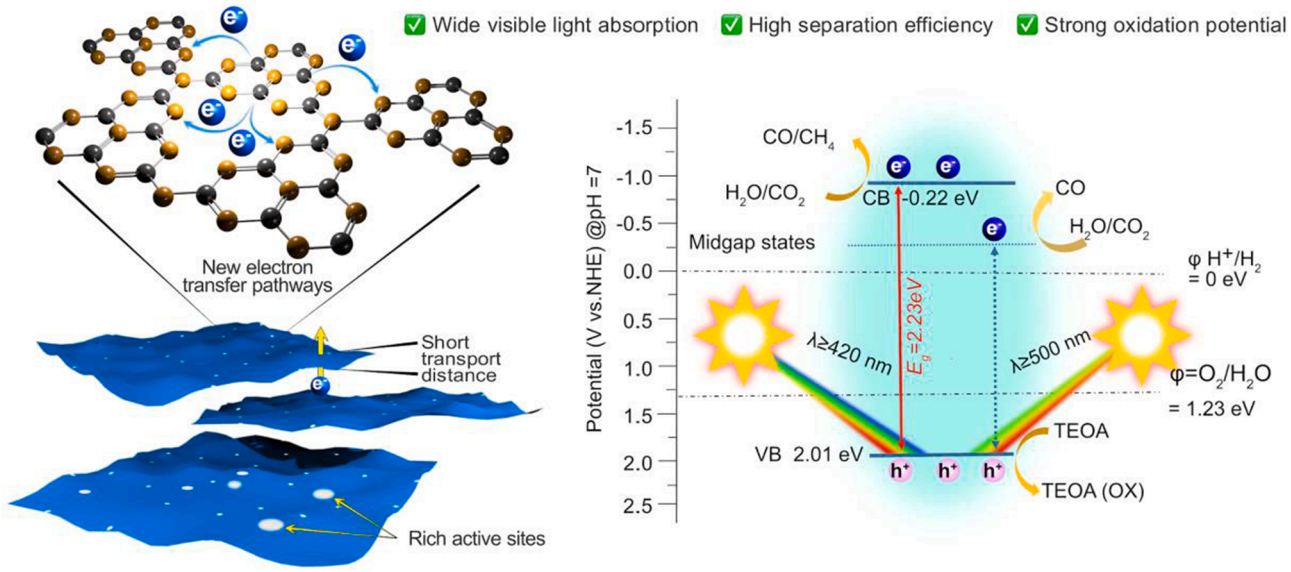

Scheme 1. Proposed mechanism of CO_2 photoreduction over UCN-620.

CO_2 to activate CO_2 and participate in the subsequent CO_2 photoreduction [53]. To gain fundamental insights into the CO_2 photoreduction mechanism, we used in-situ Fourier-transform infrared spectra (FTIR) to detect the intermediate products of UCN-620 [54]. Figure S9b shows the involvement of monodentate intermediates, including carbonate (m-CO_3^{2-}: 1316, 1337, 1458, 1518, and 1540 cm^{-1}), bidentate carbonate (b-CO_3^{2-}: 1621 and 1640 cm^{-1}), bicarbonate (HCO_3^-: 1396, 1423 and 1494 cm^{-1}), and surface formic acid (HCOOH: 1559, 1575, 1682, 1698,1744, 1773 and 1793 cm^{-1}). The corresponding intensity from these intermediates increases gradually with the illumination time.

To further illustrate the detailed CO_2 photoreduction process, there is a summary of calculated free energy (ΔG) in Figure S11. The CO_2* formation was thermodynamically favorable with a ΔG of −1.23 eV. On the other hand, the CO* formation was found to be the rate-limiting step with a ΔG of 0.74 eV. These results suggest that enhancing the COOH* to CO* conversion can further improve the photocatalytic performance.

Based on a combination of experimental observations, theoretical calculations, and literature reports, we propose a mechanism for the photoreduction of CO_2 to CO, as described by Eqs. (1) to (4). The CO_2 molecules are first absorbed on the Lewis base in the heptazine rings of g-C_3N_4. The absorbed CO_2* molecules are activated by subsequent proton-coupled electron transfer [55]. The CO_2* intermediates then couple with the resident protons, resulting in the formation of COOH* intermediates. The adsorbed CO* as the final product is generated by a subsequent proton-coupled electron transfer, followed by desorption from the surface.

$$CO_2\ (g) \rightarrow CO_2^* \quad (1)$$

$$CO_2\bullet^* + H^+ e^- \rightarrow COOH^* \quad (2)$$

$$COOH^* + H^+ e^- \rightarrow CO^* + H_2O \quad (3)$$

$$CO^* \rightarrow CO \quad (4)$$

A possible enhancement mechanism of CO_2 photoreduction for UCN-620 is now proposed based on the analysis and discussion above (see Scheme 1). Under visible light irradiation (λ ≥ 420 nm), the UCN-620 absorbs photons for electron excitation from the VB to the CB, where these photoexcited electrons boost the CO_2 to CO conversion. Meanwhile, the UCN-620, with a high oxidation potential, provides a strong driving force for the photocatalytic oxidation of TEOA. Thus, an effective reduction–oxidation occurs in the H_2O, CO_2, and TEOA systems, resulting in efficient CO_2 photoreduction.

4. Conclusion

In summary, highly polymerized ultrathin g-C_3N_4 nanosheets for visible-light-driven CO_2 photoreduction were successfully obtained via structural reorganization. These nanosheets reduce the perpendicular distance for electron migration toward the photocatalyst surface while providing high exposure to active sites. The bridged N-$(C)_3$ extends the π-conjugated system and offers more electron transfer channels, guaranteeing an efficient rapid separation and transfer of photoexcited charges. The activated n → π* electronic transitions from a buckled plane structure broadens the optical absorption to the visible spectral range. UCN-620 shows an efficient CO_2-to-CO conversion with a CO production rate of 12.95 μmol g^{-1} h^{-1} under λ ≥ 420 nm and 2 μmol g^{-1} h^{-1} under λ ≥ 500 nm visible light, respectively. This work provides a facile and clean strategy to construct a visible-light-driven ultrathin g-C_3N_4 photocatalyst opening thought-provoking insights into the structure–activity relationship for high-performance CO_2 photoreduction in a wide spectral range.

CRediT authorship contribution statement

Qian Zhang: Conceptualization, Methodology, Investigation, Writing – original draft, Visualization. **Guangfu Liao:** Investigation, Data curation, Funding acquisition, Supervision. **Bin Yang:** . **Yan Zhang:** . **Guixian Ge:** . **Anna Lipovka:** . **Jichang Liu:** . **Raul D. Rodriguez:** . **Xiaodong Yang:** . **Xin Jia:** .

Declaration of Competing Interest

The authors declare that they have no known competing financial interests or personal relationships that could have appeared to influence the work reported in this paper.

Data availability

Data will be made available on request.

Acknowledgments

This study was supported by the National Natural Science Foundation of China (U1703351, 52073179), Bingtuan Excellent Young Scholars (CZ027205), Bingtuan Science & Technology Nova, and School

of Chemistry and Chemical Engineering/State Key Laboratory Incubation Base for Green Processing of Chemical Engineering, Shihezi, 832003, China. AL and RDR acknowledge the Russian Science Foundation (23-42-00081). We would like to thank the Analysis and Testing Center of Shihezi University.

Appendix A. Supplementary data

Supplementary data to this article can be found online at https://doi.org/10.1016/j.apsusc.2023.157989.

References

[1] Y. Xu, M. Fan, W. Yang, Y. Xiao, L. Zeng, X. Wu, Q. Xu, C. Su, Q. He, Homogeneous Carbon/Potassium-Incorporation Strategy for Synthesizing Red Polymeric Carbon Nitride Capable of Near-Infrared Photocatalytic H_2 Production, Adv. Mater. 33 (2021) 2101455.
[2] X. Tang, W. Shen, D. Li, B. Li, Y. Wang, X. Song, Z. Zhu, P. Huo, Research on cobalt-doping sites in g-C_3N_4 framework and photocatalyticreduction CO_2 mechanism insights, J. Alloys Compounds 954 (2023), 170044.
[3] X. Fei, H. Tan, B. Cheng, B. Zhu, L. Zhan, 2D/2D Black Phosphorus/g-C_3N_4 S-Scheme Heterojunction Photocatalysts for CO_2 Reduction Investigated using DFT Calculations, Acta Phys. -Chim. Sin. 37 (2021) 2010027.
[4] M. Sayed, B. Zhu, P. Kuang, X. Liu, B. Cheng, A. Ghamdi, S. Wageh, L. Zhang, J. Yu, EPR Investigation on Electron Transfer of 2D/3D g-C_3N_4/ZnO S-Scheme Heterojunction for Enhanced CO_2 Photoreduction, Adv. Sust. Syst. 6 (2022) 2100264.
[5] L. Yuan, M. Qi, Z. Tang, Y. Xu, Coupling Strategy for CO_2 Valorization Integrated with Organic Synthesis by Heterogeneous Photocatalysis, Angew. Chem. Int. Ed. 60 (2021) 21150–21172.
[6] C. Han, Y. Li, J. Li, M. Qi, Z. Tang, Y. Xu, Cooperative Syngas Production and C−N Bond Formation in One Photoredox Cycle, Angew. Chem. Int. Ed. 60 (2021) 7962–7970.
[7] G. Ding, C. Li, Y. Ni, L. Chen, L. Shuai, G. Liao, Layered double hydroxides and their composites as high-performance photocatalysts for CO_2 reduction, EES Catal. 1 (2023) 369–391.
[8] J. Li, L. Yuan, S. Li, Z. Tang, Y. Xu, One-dimensional copper-based heterostructures toward photo-driven reduction of CO_2 to sustainable fuels and feedstocks, J. Mater. Chem. A 7 (2019) 8676–8689.
[9] C. Bie, B. Zhu, F. Xu, L. Zhang, J. Yu, In Situ Grown Monolayer N-Doped Graphene on CdS Hollow Spheres with Seamless Contact for Photocatalytic CO_2 Reduction, Adv. Mater. 31 (2019) 1902868.
[10] L. Yuan, Y. Xu, Photocatalytic conversion of CO_2 into value-added and renewable fuels, Appl. Surf. Sci. 342 (2015) 154–167.
[11] L. Yuan, S. Hung, Z. Tang, H. Chen, Y. Xiong, Y. Xu, Dynamic Evolution of Atomically Dispersed Cu Species for CO_2 Photoreduction to Solar Fuels, ACS Catal. 9 (2019) 4824–4833.
[12] F. Zhang, Y. Li, M. Qi, Z. Tang, Y. Xu, Boosting the activity and stability of Ag-Cu_2O/ZnO nanorods for photocatalytic CO_2 reduction, Appl. Catal. B Environ. 268 (2020), 118380.
[13] K. Lu, Y. Li, F. Zhang, M. Qi, X. Chen, Z. Tang, Y. Yamada, M. Anpo, M. Conte, Y. Xu, Rationally designed transition metal hydroxide nanosheet arrays on graphene for artificial CO_2 reduction, Nature Commun. 11 (2020) 5181.
[14] G. Liao, C. Li, X. Li, B. Fang, Emerging polymeric carbon nitride Z-scheme systems for photocatalysis, Cell Rep. Phys. Sci. 2 (2021), 100355.
[15] Y. Xu, S. Wang, J. Yang, B. Han, R. Nie, J. Wang, J. Wang, H. Jing, In-situ grown nanocrystal TiO_2 on 2D Ti_3C_2 nanosheets for artificial photosynthesis of chemical fuels, Nano Energy 51 (2018) 442–450.
[16] X. Fang, L. Ma, K. Liang, S. Zhao, Y. Jiang, C. Ling, T. Zhao, T. Cheang, A. Xu, The doping of phosphorus atoms into graphitic carbon nitride for highly enhanced photocatalytic hydrogen evolution, J. Mater. Chem. A 7 (2019) 11506–11512.
[17] M. Hussien, A. Sabbah, M. Qorbani, M. Elsayed, P. Raghunath, T. Lin, S. Quadir, H. Wang, H. Wu, D. Tzou, M. Lin, P. Chung, H. Chou, L. Chen, K. Chen, Metal-free four-in-one modification of g-C_3N_4 for superior photocatalytic CO_2 reduction and H_2 evolution, Chem. Eng. J. 430 (2022), 132853.
[18] G. Liao, Y. Gong, L. Zhang, H. Gao, G. Yang, B. Fang, Semiconductor polymeric graphitic carbon nitride photocatalysts: the 'holy grail' for the photocatalytic hydrogen evolution reaction under visible light, Energy Environ. Sci. 12 (2019) 2080–2147.
[19] B. Li, Y. Si, B. Zhou, Q. Fang, Y. Li, W. Huang, W. Hu, A. Pan, X. Fan, G. Huang, Doping-Induced Hydrogen-Bond Engineering in Polymeric Carbon Nitride To Significantly Boost the Photocatalytic H_2 Evolution Performance, ACS Appl. Mater. Interfaces 11 (2019) 17341–17349.
[20] L. Lin, Z. Yu, X. Wang, Crystalline Carbon Nitride Semiconductors for Photocatalytic Water Splitting, Angew. Chem. Int. Ed. 58 (2019) 6164–6175.
[21] Y. Kang, Y. Yang, L. Yin, X. Kang, L. Wang, G. Liu, H. Cheng, Selective Breaking of Hydrogen Bonds of Layered Carbon Nitride for Visible Light Photocatalysis, Adv. Mater. 28 (2016) 6471–6477.
[22] G. Zhang, J. Zhu, Y. Xu, C. Yang, C. He, P. Zhang, Y. Li, X. Ren, H. Mi, In-Plane Charge Transport Dominates the Overall Charge Separation and Photocatalytic Activity in Crystalline Carbon Nitride, ACS Catal. 12 (2022) 4648–4658.
[23] L. Lin, Z. Yu, X. Wang, Crystalline Carbon Nitride Semiconductors for Photocatalytic Water Splitting, Angew. Chem. Int. Ed. 131 (2019) 6225–6236.
[24] H. Ou, L. Lin, Y. Zheng, P. Yang, Y. Fang, X. Wang, Tri-s-triazine-Based Crystalline Carbon Nitride Nanosheets for an Improved Hydrogen Evolution, Adv. Mater. 29 (2017) 1700008.
[25] L. Lin, W. Ren, C. Wang, A. Asiri, J. Zhang, X. Wang, Crystalline carbon nitride semiconductors prepared at different temperatures for photocatalytic hydrogen production, Appl. Catal. B: Environ. 231 (2018) 234–241.
[26] W. Iqbal, B. Qiu, Q. Zhu, M. Xing, J. Zhang, Self-modified breaking hydrogen bonds to highly crystalline graphitic carbon nitrides nanosheets for drastically enhanced hydrogen production, Appl. Catal. B: Environ. 232 (2018) 306–313.
[27] S. An, G. Zhang, K. Li, Z. Huang, X. Wang, Y. Guo, J. Hou, C. Song, X. Guo, Self-Supporting 3D Carbon Nitride with Tunable n→π* Electronic Transition for Enhanced Solar Hydrogen Production, Adv. Mater. 33 (2021) 2104361.
[28] Y. Chen, B. Wang, S. Lin, Y. Zhang, X. Wang, Activation of n → π* Transitions in Two-Dimensional Conjugated Polymers for Visible Light Photocatalysis, J. Phys. Chem. C 118 (2014) 29981–29989.
[29] G. Zhang, A. Savateev, Y. Zhao, L. Li, M. Antonietti, Advancing the n→π* electron transition of carbon nitride nanotubes for H_2 photosynthesis, J. Mater. Chem. A (2017) 12723–12728.
[30] S. Hu, D. Jiang, L. Gu, G. Xu, Z. Li, Y. Yuan, Awakening n→π* electronic transition by breaking hydrogen bonds in graphitic carbon nitride for increased photocatalytic hydrogen generation, Chem. Eng. J. 399 (2020), 125847.
[31] Q. Yang, W. Yang, F. He, K. Liu, H. Cao, H. Yan, One-step synthesis of nitrogen-defective graphitic carbon nitride for improving photocatalytic hydrogen evolution, J. Hazard. Mater. 410 (2021), 124594.
[32] L. Liu, F. Chen, J. Wu, M. Ke, C. Cui, J. Chen, H. Yu, Edge electronic vacancy on ultrathin carbon nitride nanosheets anchoring O_2 to boost H_2O_2 photoproduction, Appl. Catal. B: Environ. 302 (2022), 120845.
[33] D. Zhao, J. Chen, C. Dong, W. Zhou, Y. Huang, S. Mao, L. Guo, S. Shen, Interlayer interaction in ultrathin nanosheets of graphitic carbon nitride for efficient photocatalytic hydrogen evolution, J. Catal. 352 (2017) 491–497.
[34] B. Yang, J. Zhao, W. Yang, X. Sun, R. Wang, X. Jia, A step-by-step synergistic stripping approach toward ultra-thin porous g-C_3N_4 nanosheets with high conduction band position for photocatalystic CO_2 reduction, J. Colloid Interface Sci. 589 (2021) 179–186.
[35] B. Yang, Z. Wang, J. Zhao, X. Sun, R. Wang, G. Liao, X. Jia, 1D/2D carbon-doped nanowire/ultra-thin nanosheet g-C_3N_4 isotype heterojunction for effective and durable photocatalytic H_2 evolution, Int. J. Hydrogen Energy 46 (2021) 25436–25447.
[36] J. Bai, L. Wang, Y. Zhang, C. Wen, X. Wang, H. Yang, Carboxyl functionalized graphite carbon nitride for remarkably enhanced photocatalytic hydrogen evolution, Appl. Catal. B: Environ. 266 (2020), 118590.
[37] W. Tu, Y. Xu, J. Wang, B. Zhang, T. Zhou, S. Yin, S. Wu, C. Li, Y. Huang, Y. Zhou, Z. Zou, J. Robertson, M. Kraft, R. Xu, Investigating the Role of Tunable Nitrogen Vacancies in Graphitic Carbon Nitride Nanosheets for Efficient Visible-Light-Driven H_2 Evolution and CO_2 Reduction, ACS Sustainable Chem. Eng. 5 (2017) 7260–7268.
[38] X. Wang, J. Meng, X. Zhang, Y. Liu, M. Ren, Y. Yang, Y. Guo, Controllable Approach to Carbon-Deficient and Oxygen-Doped Graphitic Carbon Nitride: Robust Photocatalyst Against Recalcitrant Organic Pollutants and the Mechanism Insight, Adv. Funct. Mater. 31 (2021) 2010763.
[39] Y. Xue, Y. Guo, Z. Liang, H. Cui, J. Tian, Porous g-C_3N_4 with nitrogen defects and cyano groups for excellent photocatalytic nitrogen fixation without co-catalysts, J. Colloid Interface Sci. 556 (2019) 206–213.
[40] W. Li, Z. Guo, L. Jiang, L. Zhong, G. Li, J. Zhang, K. Fan, S. Gonzalez-Cortes, K. Jin, C. Xu, T. Xiao, P.P. Edwards, Facile in situ reductive synthesis of both nitrogen deficient and protonated g-C_3N_4 nanosheets for the synergistic enhancement of visible-light H_2 evolution, Chem. Sci. 11 (2020) 2716–2728.
[41] Q. Zhang, P. Chen, C. Tan, T. Chen, M. Zhuo, Z. Xie, F. Wang, H. Liu, Z. Cai, G. Liu, W. Lv, A photocatalytic degradation strategy of PPCPs by a heptazine-based CN organic polymer (OCN) under visible light, Environ. Sci.: Nano 5 (2018) 2325–2336.
[42] P. Kumar, E. Vahidzadeh, U.K. Thakur, P. Kar, K.M. Alam, A. Goswami, N. Mahdi, K. Cui, G.M. Bernard, V.K. Michaelis, K. Shankar, C3N5: A Low Bandgap Semiconductor Containing an Azo-linked Carbon Nitride Framework for Photocatalytic, Photovoltaic and Adsorbent Applications, J. Am. Chem. Soc. 141 (2019) 5415–5436.
[43] D. Zhao, C. Dong, B. Wang, C. Chen, Y. Huang, Z. Diao, S. Li, L. Guo, S. Shen, Synergy of Dopants and Defects in Graphitic Carbon Nitride with Exceptionally Modulated Band Structures for Efficient Photocatalytic Oxygen Evolution, Adv. Mater. 31 (2019) 1903545.
[44] C. Liang, H. Niu, H. Guo, C. Niu, D. Huang, Y. Yang, H. Liu, B. Shao, H. Feng, Insight into Photocatalytic Nitrogen Fixation on Graphitic Carbon Nitride: Defect-Dopant Strategy of Nitrogen Defect and Boron Dopant, Chem. Eng. J. 396 (2020), 125395.
[45] M. Ren, X. Zhang, Y. Liu, G. Yang, L. Qin, J. Meng, Y. Guo, Y. Yang, Interlayer Palladium-Single-Atom-Coordinated Cyano-Group-Rich Graphitic Carbon Nitride for Enhanced Photocatalytic Hydrogen Production Performance, ACS Catal. 12 (2022) 5077–5093.
[46] L. Shi, T. Wang, H. Zhang, K. Chang, J. Ye, Electrostatic Self-Assembly of Nanosized Carbon Nitride Nanosheet onto a Zirconium Metal-Organic Framework for Enhanced Photocatalytic CO_2 Reduction, Adv. Funct. Mater. 25 (2015) 5360–5367.
[47] C. Han, P. Su, B. Tan, X. Ma, H. Lv, C. Huang, P. Wang, Z. Tong, G. Li, Y. Huang, Defective ultra-thin two-dimensional g-C_3N_4 photocatalyst for enhanced photocatalytic H_2 evolution activity, J. Colloid Interface Sci. 581 (2021) 159–166.

[48] Y. Liu, S. Zhao, C. Zhang, J. Fang, L. Xie, Y. Zhou, S. Zhuo, Hollow tubular carbon doping graphitic carbon nitride with adjustable structure for highly enhanced photocatalytic hydrogen production, Carbon 182 (2021) 287–296.
[49] R. Wang, P. Yang, S. Wang, X. Wang, Distorted carbon nitride nanosheets with activated n→π* transition and preferred textural properties for photocatalytic CO_2 reduction, J. Catal. 402 (2021) 166–176.
[50] S. Li, G. Dong, R. Hailili, L. Yang, Y. Li, F. Wang, Y. Zeng, C. Wang, Effective photocatalytic H_2O_2 production under visible light irradiation at g-C_3N_4 modulated by carbon vacancies, Appl. Catal. B Environ. 190 (2016) 26–35.
[51] Y. Li, W. Ho, K. Lv, B. Zhu, S.C. Lee, Carbon vacancy-induced enhancement of the visible light-driven photocatalytic oxidation of NO over g-C_3N_4 nanosheets, Appl. Surf. Sci. 403 (2018) 380–389.
[52] B. Yang, X. Li, Q. Zhang, X. Yang, J. Wan, G. Liao, J. Zhao, R. Wang, J. Liu, R. D. Rodriguez, X. Jia, Ultrathin Porous Carbon Nitride Nanosheets with Well-tuned Band Structures via Carbon Vacancies and Oxygen Doping for Significantly Boosting H_2 Production, Appl. Catal. B Environ. 314 (2022), 121521.
[53] Z. Sun, H. Wang, Z. Wu, L. Wang, g-C_3N_4 based composite photocatalysts for photocatalytic CO_2 reduction, Catal. Today 300 (2018) 160–172.
[54] Z. Ma, P. Li, L. Ye, Y. Zhou, F. Su, C. Ding, H. Xie, Y. Bai, P.K. Wong, Oxygen vacancies induced exciton dissociation of flexible BiOCl nanosheets for effective photocatalytic CO_2 conversion, J. Mater. Chem. A 5 (2017) 24995–25004.
[55] S. Gong, X. Teng, Y. Niu, X. Liu, M. Xu, C. Xu, L. Ji, Z. Chen, Construction of S-scheme 0D/2D heterostructures for enhanced visible-light-driven CO_2 reduction, Appl. Catal. B Environ. 298 (2021) 120521.